

# Nanoconfinement controls stiffness, strength and mechanical toughness of $\beta$ -sheet crystals in silk

Sinan Keten<sup>1</sup>, Zhiping Xu<sup>1,2</sup>, Britni Ihle<sup>1</sup> and Markus J. Buehler<sup>1,2,3\*</sup>

**Silk features exceptional mechanical properties such as high tensile strength and great extensibility, making it one of the toughest materials known. The exceptional strength of silkworm and spider silks, exceeding that of steel, arises from  $\beta$ -sheet nanocrystals that universally consist of highly conserved poly-(Gly-Ala) and poly-Ala domains. This is counterintuitive because the key molecular interactions in  $\beta$ -sheet nanocrystals are hydrogen bonds, one of the weakest chemical bonds known. Here we report a series of large-scale molecular dynamics simulations, revealing that  $\beta$ -sheet nanocrystals confined to a few nanometres achieve higher stiffness, strength and mechanical toughness than larger nanocrystals. We illustrate that through nanoconfinement, a combination of uniform shear deformation that makes most efficient use of hydrogen bonds and the emergence of dissipative molecular stick-slip deformation leads to significantly enhanced mechanical properties. Our findings explain how size effects can be exploited to create bioinspired materials with superior mechanical properties in spite of relying on mechanically inferior, weak hydrogen bonds.**

Silk is a biological protein fibre with exceptional tunable mechanical properties such as high tensile strength and great extensibility, making it one of the toughest and most versatile materials known<sup>1–3</sup>. Since its development in China thousands of years ago, silk has been used throughout history not only as luxury fabrics but also in various technological applications including parachutes, medical sutures and, more recently, tissue regeneration<sup>4</sup>. Variations in synthesis conditions such as temperature, reeling speed and pH lead to silk-based peptide fibrils or protein aggregates with rather different structural and mechanical properties<sup>5–8</sup>. However, despite decades of research in silk production and mechanical properties, the mass production of silk and biomimetic materials remains a challenge, particularly because of silk's unique features that can be achieved only by the controlled self-assembly of the macromolecular constructs with molecular precision at the nanoscale.

Recent investigations revealed that antiparallel  $\beta$ -sheet crystals at the nanoscale, consisting of highly conserved poly-(Gly-Ala) and poly-Ala repeats found in both commercial and spider silk<sup>9</sup>, have a key role in defining the mechanical properties of silk by providing stiff orderly crosslinking domains embedded in a semi-amorphous matrix that consists predominantly of less orderly  $\beta$ -structures,  $3_1$  helices and  $\beta$ -turns<sup>10–12</sup> (Fig. 1a).  $\beta$ -sheet nanocrystals, bonded by means of assemblies of hydrogen bonds<sup>13,14</sup>, have dimensions of a few nanometres and constitute roughly 10–15% of the silk volume, whereas with less orderly extended structures the  $\beta$ -sheet content can exceed 50% for spider and silkworm silks<sup>6,15,16</sup>. When silk fibres are exposed to stretch,  $\beta$ -sheet nanocrystals reinforce the partially extended and oriented macromolecular chains by forming interlocking regions that transfer the load between chains under lateral loading, similar to their function in other mechanical proteins<sup>10,17–23</sup>. Thereby,  $\beta$ -sheet nanocrystals provide cohesion between the long polypeptide strands, enabling the amorphous domains to stretch significantly. Eventually, fracture of  $\beta$ -sheet nanocrystals occurs at large deformation and large loads, where the typical loading at individual  $\beta$ -sheet nanocrystals is lateral<sup>9</sup>.

Recent experiments demonstrated that when the size of  $\beta$ -sheet nanocrystals is reduced by moderating the reeling speed or by metal infiltration, silk shows enhanced toughness and greater ultimate strength<sup>5–7</sup>, exceeding that of steel and other engineered materials. This is particularly intriguing because hydrogen bonds comprise the chemical bonds that underlie the  $\beta$ -sheet nanocrystal structures, and are one of the weakest chemical bonds known. The issue of how hydrogen-bonded silk threads can reach such great strength and toughness to overcome the limitations of their inferior building blocks is a question of fundamental importance to understanding the behaviour of a broader class of  $\beta$ -sheet-rich biological protein materials (for example, amyloids,  $\beta$ -solenoids, virulence factors).

To address this issue, the investigation of the properties of silk  $\beta$ -sheet nanocrystals requires an accurate representation of the protein's amino-acid sequence and chemical interactions from a bottom-up perspective. This renders explicit water molecular dynamics a suitable tool, as it provides an accurate description of the physical mechanisms governing self-assembly (association) and failure (dissociation) of polypeptide chains at submicrometre length scales<sup>23–27</sup>. Here we focus on  $\beta$ -sheet nanocrystals using the sequence from *Bombyx mori* silk<sup>28</sup> as a model system, which is representative of the structure of nanocrystals found in silks from most spider and silkworm species because of the extremely high sequence conservation of the crystalline regions (consisting of (Gly-Ala)<sub>N</sub> or (Ala)<sub>N</sub> repeats with 6–10 residues).

To examine the key mechanical parameters of the silk  $\beta$ -sheet nanocrystals as a function of size, we carry out two sets of computational experiments, namely bending and pull-out simulations. The choice of this set-up is motivated by our desire to create a model system to quantify the size-dependent lateral stiffness of silk  $\beta$ -sheet nanocrystals under lateral loading, which is the key loading condition of nanocrystals in silk<sup>29–31</sup>. In the bending scenario (Fig. 1b), a constant lateral force is applied at one end of the nanocrystal while the other end remains fixed, resembling a cantilever beam with tip loading (see Fig. 1a). This set-up mimics biological assays used in single-molecule experiments to

<sup>1</sup>Laboratory for Atomistic and Molecular Mechanics, Department of Civil and Environmental Engineering, Massachusetts Institute of Technology, 77 Massachusetts Avenue, Room 1-235A&B, Cambridge, Massachusetts 02139, USA, <sup>2</sup>Center for Materials Science and Engineering, Massachusetts Institute of Technology, 77 Massachusetts Avenue, Cambridge, Massachusetts 02139, USA, <sup>3</sup>Center for Computational Engineering, Massachusetts Institute of Technology, 77 Massachusetts Avenue, Cambridge, Massachusetts 02139, USA. \*e-mail: mbuehler@MIT.EDU.

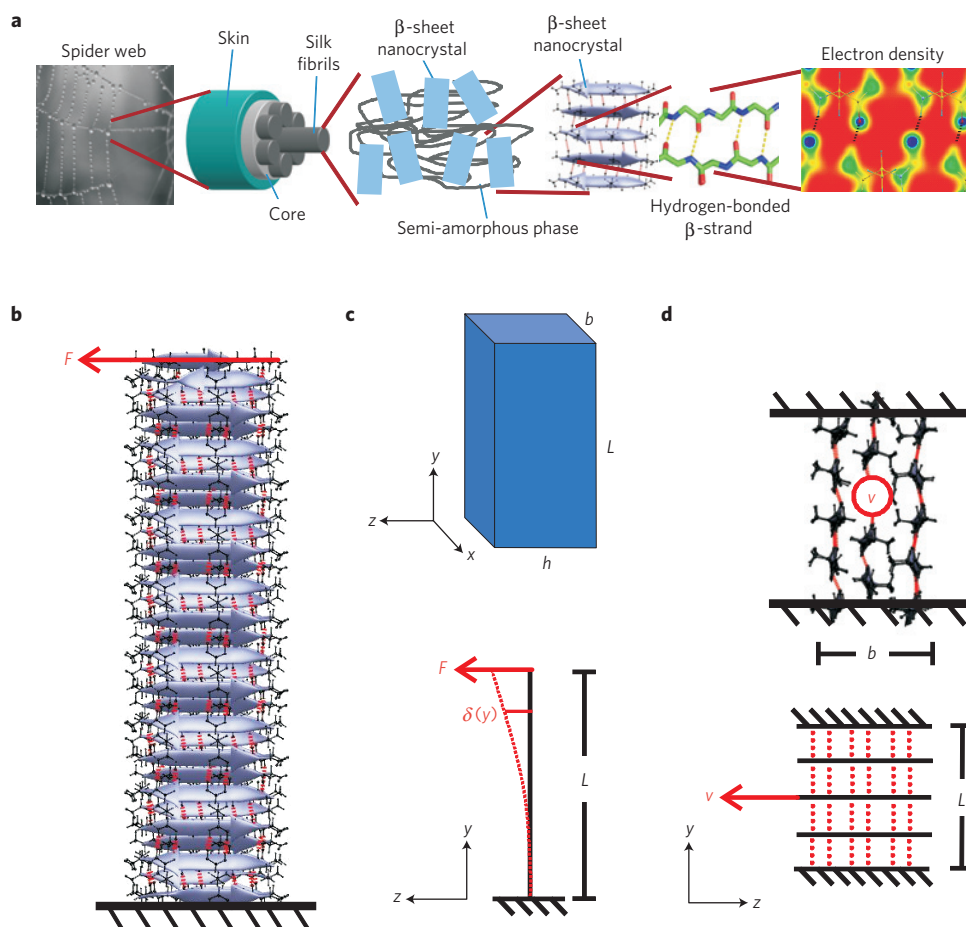


**Figure 1 | Hierarchical structure of spider silk, simulation set-up and theoretical considerations.** **a**, Schematic of the hierarchical spider silk structure that ranges from nano to macro. **a** displays key structural features of silk, including the electron density at the Angstrom scale, hydrogen bonded  $\beta$ -strands,  $\beta$ -sheet nanocrystals, a hetero-nanocomposite of stiff nanocrystals embedded in a softer semi-amorphous phase and silk fibrils, which assembles into macroscopic silk fibres. **b**, The atomistic structure of the silk  $\beta$ -sheet nanocrystal obtained from the Protein Data Bank (identification code 2slk) and replicated to build  $\beta$ -sheet nanocrystals of different sizes. In the first set of simulations, the  $\beta$ -sheet nanocrystal is subject to loading conditions similar to a cantilever beam with a constant tip loading, used to identify the bending rigidity and other structural properties. This loading mimics the characteristic lateral loading relevant to silk mechanics. **c**, Schematic representation of the  $\beta$ -sheet nanocrystal and definition of coordinates used here (upper part, where parameters  $b$  and  $h$  describe geometric parameters related to the number of sheets and the length of strands in the nanocrystal, and  $L$  is the size of the nanocrystal in the  $y$  direction). The lower part shows the geometry of the bending study and defines the displacement variable. **d**, Set-up for pull-out simulations, where to characterize fracture resistance of the nanocrystals, the central strand of the middle sheet is pulled out with constant velocity, while the top and bottom strands are restrained.

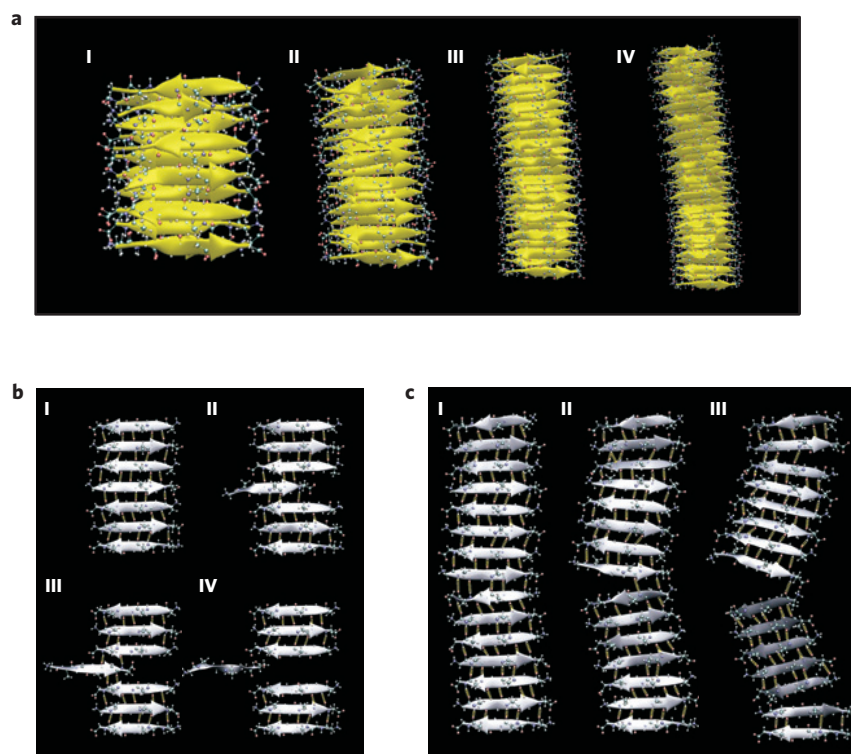
assess mechanical properties (for example, elastic moduli) or the persistence length of biofilaments<sup>32,33</sup>. In the pull-out scenario (Fig. 1d), the centre strand of the assembly is pulled out while the outermost ends of the nanocrystal are fixed, to assess the deformation and fracture behaviour of the system at large forces. The pull-out set-up complements the first one by revealing the strength, fracture toughness and molecular failure mechanisms of nanocrystals as a function of their size.

Figure 2a shows snapshots from bending studies where the constant force applied laterally at the tip of the  $\beta$ -sheet nanocrystal scales with its size. Forces of  $F = 375$  pN,  $F = 215$  pN,  $F = 135$  pN and  $F = 100$  pN are applied for the smallest to largest nanocrystal sizes  $L = 1.87$  nm,  $L = 3.31$  nm,  $L = 5.18$  nm and  $L = 7.04$  nm, to obtain reasonable displacements in each case. A softening of the system in larger nanocrystals is evident from snapshots of deformation, which increases as the size of the nanocrystal increases. The scaling of the stiffness is first compared with a classical Euler–Bernoulli beam theory (equation (2)) commonly applied to biological filaments and nanostructures<sup>34</sup>. We observe that this model shows a significant disagreement when the stiffness

of the nanocrystal is plotted against size, and thus fails to properly describe the simulation results shown in Fig. 3a. This is because shear deformations are neglected in this classical beam theory, as it considers only tensile and compressive stresses in a beam's cross-section. On inclusion of shear contributions<sup>34</sup> (equations (3) and (4)), the agreement between simulation and beam theory is excellent, as shown in Fig. 3a (for details, see the Methods section and Supplementary Information). The comparison of the simulation results with the two models suggests that the disagreement arises from the shear contribution to deformation, which is neglected in the conventional theory but is apparently critical in describing the deformation mechanisms in  $\beta$ -sheet nanocrystals.

Moreover, the series of nanomechanical experiments enables us to identify the distribution of strains in the nanocrystal. The relative importance of shear contributions in the deformation of a  $\beta$ -sheet nanocrystal of size  $L$  is given by the shear contribution ratio

$$s(L) = \frac{3D_B}{L^2 D_T} = \frac{1}{4} \frac{Eh^2}{GL^2} \sim \frac{h^2}{L^2} \quad (1)$$



**Figure 2 | Snapshots of deformation profiles and failure mechanisms of silk  $\beta$ -sheet nanocrystals at different sizes.** **a**, Size-dependent elastic deformation of  $\beta$ -sheet nanocrystals, based on simulations in the bending set-up under lateral loading (Fig. 1b,c). Smaller structures show a linear displacement profile, in line with shear-governed deformation, whereas a nonlinear profile with a significantly higher curvature is observed for longer structures, illustrating a transition from shear- to bending-governed deformation. **b,c**, Fracture mechanism during pull-out simulations (lateral loading condition shown in Fig. 1d). The  $\beta$ -sheet nanocrystal sizes investigated here range from 2 to 7 nm. **b** shows a visualization of the failure mechanism in a  $\beta$ -sheet nanocrystal using seven strands ( $L = 2.83$  nm), with snapshots taken just before and after failure by rupture of hydrogen bonds. **c** depicts the molecular failure mechanism of the largest  $\beta$ -sheet nanocrystal studied ( $L = 6.56$  nm), with snapshots taken just before and after failure by rupture of hydrogen bonds. The main difference in the failure mechanism between the cases shown in **b** and **c** is that longer structures fail by significant bending, which leads to a crack-like flaw formation owing to non-uniform tensile deformation of hydrogen bonds. In the case of shorter structures as shown in **b**, the system responds more rigidly (stiffer), and hydrogen bonds break by means of a stick-slip motion owing to uniform shear loading. The stick-slip failure mode leads to significantly enhanced energy dissipation and multiple force peaks in the force-displacement curve (see Fig. 4a).

where the terms  $D_B = EI$  and  $D_T = GA_s$  denote the bending and shear rigidity, respectively. In this notation,  $E$  and  $G$  stand for elastic and shear moduli, respectively, and  $A_s$  is the cross-sectional area. For a rectangular cross-section (Fig. 1c), the moment of inertia  $I = bh^3/12$  and  $A_s = bh$ , where  $b$  is the base length (related here to the number of sheets) and  $h$  is the height of the cross-section (related here to the length of a  $\beta$ -strand). The shear contribution ratio  $s$  plotted as a function of size shown in Fig. 3b illustrates that as the size of the nanocrystal gets smaller, the loading scenario becomes predominantly shear ( $s > 1$ ), whereas for large  $\beta$ -sheet nanocrystals pure bending controls deformation ( $s < 1$ ). The existence of this important size effect is independent of the particular boundary conditions and is a result purely of the geometry and the material properties of  $\beta$ -sheet nanocrystals.

This change in stress distribution inside the nanocrystal has significant implications on how individual hydrogen bonds are loaded. When  $s < 1$ , hydrogen bonds are stretched in tension (that is, pulled in the bonding direction). In contrast, when  $s > 1$ , hydrogen bonds are being sheared (that is, pulled orthogonal to the bonding direction). For the smallest system considered here ( $L = 1.87$  nm), the shear contribution is twice that of bending, whereas for the largest system ( $L = 7.04$  nm), shear contributes less than 10% to the total deformation. By defining a critical shear contribution ratio  $s^* = 1$ , we identify a critical shear transition length scale  $L^* \approx 2.5$  nm. As both  $D_B$  and  $D_T$  scale linearly with the number of sheets (that is,

the dimension  $b$  along the  $x$  axis as shown in Fig. 1c), the shear contribution ratio  $s$  is independent of variations of  $b$ . Figure 3c shows displacement profiles for each case, where the continuous curves illustrate the continuum theory predictions that include both bending and shear. The inset shows the deviation of the tip displacement by considering the difference between the model that incorporates shear and bending, and a model that incorporates only shear. This analysis directly shows that bending dominates deformation for large  $\beta$ -sheet nanocrystals, and shear dominates deformation for small  $\beta$ -sheet nanocrystals, confirming the results discussed above.

In addition to the analysis of the significance of shear contributions as a function of the nanocrystal size, the elastic and shear moduli of the material can be estimated from  $D_B$  and  $D_T$ . We find that the shear modulus  $G = 4.6$  GPa and the elastic modulus  $E = 22.6$  GPa. We carry out density functional theory (DFT) calculations that confirm this result, leading to  $G = 10.32$  GPa and  $E = 36.45$  GPa. The DFT results are slightly higher, as expected for static calculations at zero temperature. Most importantly, our findings agree very well with reported experimental values of the elastic modulus of spider-silk nanocrystals, where values in the range of  $E = 16$ – $28$  GPa have been reported<sup>35,36</sup> (see Table 1 for an overview). This direct comparison between our simulation results and experiments provides validation for our simulation approach. The shear modulus of silk  $\beta$ -sheet nanocrystals has not been tested directly, but results from torsion experiments on silk fibres

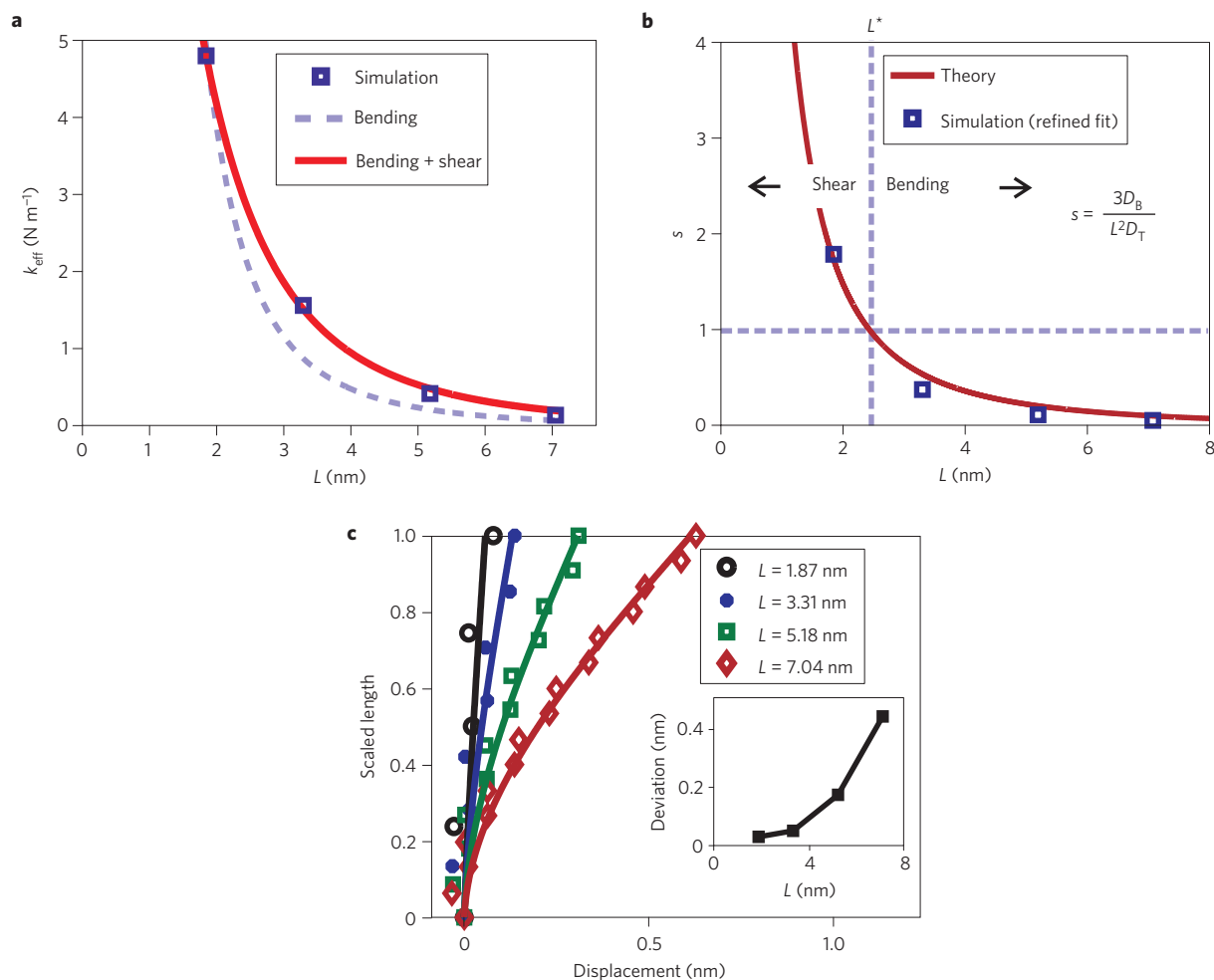


**Figure 3 | Size dependence of the stiffness, and bending versus shear contributions as a function of  $\beta$ -sheet nanocrystal size.** **a**, Effective stiffness of the beam, calculated from the ratio of force applied to the observed time average of displacement at the tip. When only bending deformation is taken into account, large deviations between the model and simulation results are observed. When shear contributions to deformation are incorporated into the model (combined bending/shear model), the agreement of the overall data with continuum theory is significantly improved. **b**, Ratio of bending to shear contributions (defined as the shear contribution ratio  $s$ ), as a function of  $\beta$ -sheet nanocrystal size  $L$ . For the smallest system studied, the shear contribution is twice that of bending, whereas for the longest system, shear contributes less than 10% to the total deformation. **c**, Displacement profiles for each case, where the continuous curves illustrate the continuum theory calculations that include both bending and shear and have been fitted to each profile with refinements to the estimated material constants. The discrete data points in **b** show the  $s$  ratios obtained for each case, based on the refined  $D_B$  and  $D_T$  parameters extracted from entire displacement profile curves (see Methods and Supplementary Information for details). Good agreement of the shear contribution ratio  $s$  with the fit from Fig. 3a (red curve in **b**) with refined values (discrete points in **b**) is found, suggesting that the shear contribution ratios do not vary significantly whether a refined fit or an overall fit is used. The inset in **c** shows the deviation of the tip displacement, by considering the difference between the model that considers shear and bending, and the model that incorporates only shear. The plots show that the deviation approaches zero for the small nanocrystals where shear displacement dominates. In contrast, the deviation increases for large nanocrystals, showing that once the crystal size exceeds a critical size, bending deformation becomes more important.

suggested shear moduli of 2.38 GPa for *Nephila clavipes* dragline silk and 3.81 GPa for *B. mori* silk<sup>37</sup>, in a similar range as our findings.

The change in the distribution of strains in a nanocrystal as a function of its size is expected to have important repercussions on its ultimate fracture behaviour under extreme loads. This is due to the fact that hydrogen bonds are loaded in tension in large crystals, whereas they are loaded in shear in small nanocrystals. As hydrogen bonds are known to be significantly weaker in non-uniform tension than in uniform shear<sup>20</sup>, they consequently feature a greatly varied capacity to withstand deformation. To test this hypothesis, we assess the failure mechanisms of  $\beta$ -sheet nanocrystals by carrying out pull-out simulations (Fig. 1d), used here to examine the ultimate strength, elastic energy storage (resilience) and energy dissipation (toughness) capacity of  $\beta$ -sheet nanocrystals under variations of the  $\beta$ -sheet nanocrystal size  $L$ . Force–displacement curves are

shown in Fig. 4a for varying nanocrystal sizes. As can be inferred from Fig. 4a,b, both the initial stiffness and the ultimate strength (maximum force peak) reach significantly larger values as the system size decreases below roughly 3 nm. Notably, the toughness is also maximized for systems beyond roughly 3 nm as shown in Fig. 4c. The length scale at which the changes in the material behaviour occur is strikingly similar to the critical crystal size estimated above,  $L^* \approx 2.5$  nm, corroborating our hypothesis that the change in the strain distribution in the nanocrystals has significant implications on their fracture behaviour as the capacity of hydrogen bonds to resist mechanical loads is altered.

The molecular mechanisms that lead to this behaviour are evident from force–displacement graphs and an analysis of the molecular trajectories. In the case of small systems, the molecular assembly is stiff, and the initial rupture is followed by a stick–slip

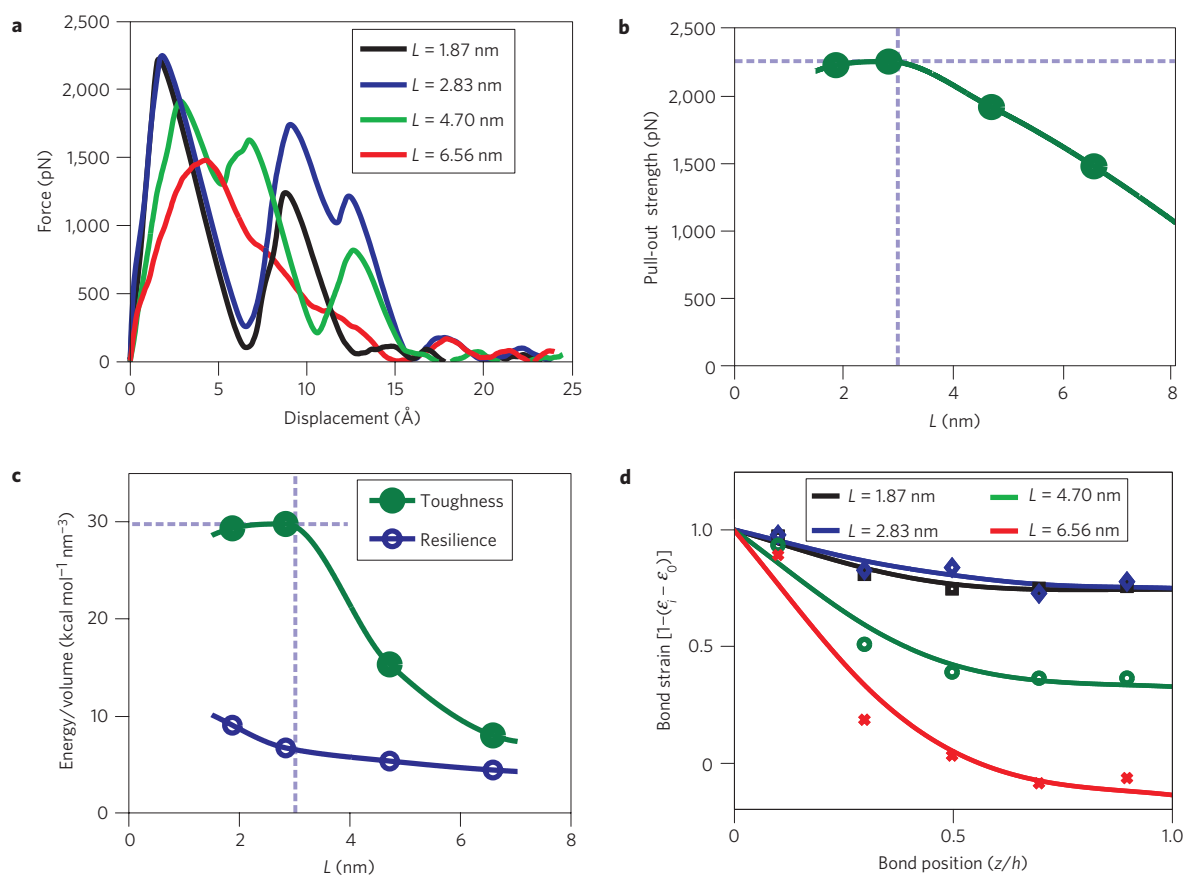


**Figure 4 | Strength, toughness, resilience and strain distribution in  $\beta$ -sheet nanocrystals as a function of crystal size.** Here we present results from pull-out simulations. **a**, Force–displacement profiles. **b**, Variation of pull-out strength as a function of  $\beta$ -sheet nanocrystal size  $L$ . **c**, Toughness and resilience as a function of  $\beta$ -sheet nanocrystal size  $L$ . As shown in **a**, smaller nanocrystals show multiple force peaks owing to a slip-stick motion that can take place only when the interacting surfaces in  $\beta$ -sheet nanocrystals, adjacent  $\beta$ -strands, are rigidly stabilized and act cooperatively. The position of the initial force peak depends not only on absolute deformation of the hydrogen-bonds but also on the total deflection of the system, which increases slightly with increasing nanocrystal size (as the effective stiffness decreases following the trend shown in Fig. 3a). The distance between the force peaks confirms that the stick-slip mechanism occurs by breaking and reformation of hydrogen-bond rings, corresponding to either approximately 0.38 nm or 0.75 nm distance between multiple force peaks. The force peak distance of 0.38 nm occurs when the strand rotates and forms new bonds, and the force peak distance of 0.75 nm corresponds to the case where the  $\beta$ -strand shifts to the next hydrogen-bond ring while preserving the direction of side chains. The stiffer failure response of the system leads to higher pull-out forces and thus greater strengths (**b**) and significantly enhanced energy dissipation owing to the slip-stick failure mechanism (**c**). The significance of this atomistic mechanism is evident from **c**, where the representative toughness of the system is calculated as the area under the force–displacement curve. The results suggest that smaller  $\beta$ -sheet nanocrystals are capable of dissipating significantly more energy during failure, which results in a high fracture toughness. Similarly, the resilience of the system—defined as the energy stored just before the initial rupture of hydrogen bonds—is also greater for smaller sized systems. **d**, Analysis of internal strain distribution in the  $\beta$ -sheet nanocrystal, as a function of crystal size. The plot shows the normalized hydrogen-bond strain over  $z/h$ , for different nanocrystal dimensions (load applied at  $z/h = 0$ ). These data clearly show that the strain distribution becomes more homogeneous for small nanocrystals, but show significant strain localization in large nanocrystals. The dashed lines illustrate the length scales below which cooperation of the hydrogen bonds is ensured through shear-dominated loading, in agreement with bending simulations presented in Fig. 3. The smooth lines in **b**, **c**, **d** are spline fits to the data for guidance.

motion as the strand slides and reforms hydrogen bonds. The distances between force peaks confirm that hydrogen bonds break and reform at the adjacent hydrogen-bond ring, either preserving the side-chain orientation and shifting approximately 0.75 nm, or by rotating and forming an opposite side-chain orientation by shifting approximately 0.38 nm. This leads to several force peaks in the mechanical response (see Fig. 4a), which significantly increases the total dissipated energy. Similarly, the resilience of the system, defined here as the elastic energy stored in the linear regime preceding the first rupture event, also becomes greater as the size is decreased, as shown in Fig. 4c. The molecular mechanism that leads to this change is directly evident from Fig. 4d, which shows the strain distribution of hydrogen bonds along the section of the pulled strand preceding failure. As the size of the nanocrystal is reduced below roughly 3 nm, the strain distribution becomes increasingly

uniform and approaches an almost constant value throughout the entire section of the nanocrystal. The constant level of strain throughout small nanocrystals leads to homogeneous shear failure, in agreement with the observations reported in Fig. 2b. In contrast, the strain concentration that emerges at the loading point in large nanocrystals results in the formation of crack-like flaws that initiate catastrophic failure even at small loads, as shown in Fig. 2c.

An important implication of the model involves the length of individual  $\beta$ -strands, represented by the parameter  $h$  (see Fig. 1c). The strand length  $h$  is proportional to the number of amino acids in a  $\beta$ -strand, as  $h = NL_0$  (where  $L_0 \approx 3 \text{ \AA}$  is the  $C_\alpha$ -distance along a  $\beta$ -strand and  $N$  denotes the number of amino acids in a  $\beta$ -strand). As  $s \approx h^2/L^2$  (equation (1)), the shear contribution ratio  $s$  is expected to be higher for nanocrystals composed of longer  $\beta$ -strands, leading to a greater shear contribution for a

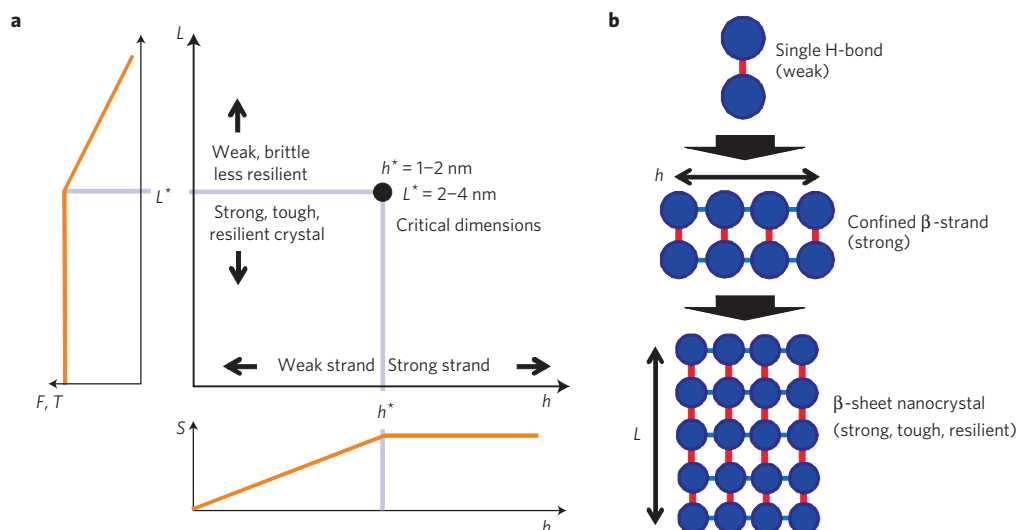


**Figure 5 | Hierarchical effects in the architecture of spider silk nanocrystals.** The formation of confined  $\beta$ -sheet nanocrystals with critical strand length  $h^*$  and critical nanocrystal size  $L^*$  provides maximum strength, toughness and stiffness. **a**, Schematic phase diagram to show the interplay of the parameters  $h$  and  $L$  in defining the properties of nanocrystals ( $S$  = schematic plot of the strength of a  $\beta$ -strand as a function of strand length  $h$  (for details, see refs 13, 38),  $F$  = strength of nanocrystal as a function of crystal size  $L$ ,  $T$  = toughness of nanocrystal as a function of crystal size  $L$ ; both plotted schematically based on the results shown in Fig. 4). Although increasing the number of hydrogen bonds in a  $\beta$ -strand increases its mechanical stability for small numbers of hydrogen bonds, the effect does not continue for  $\beta$ -strands that contain more than roughly 4 hydrogen bonds, resulting in a plateau of the strength  $S$  for lengths in excess of  $h^*$ . The physics behind this observation is a localization of deformation, similar to localization of shear slip in a crystal when dislocations are formed<sup>13,38–42</sup>. **b**, Schematic illustration of how hierarchical structure formation in the strand length  $h$  and nanocrystal size  $L$  lead to the formation of high-performance  $\beta$ -sheet nanocrystals that combine strength, toughness and resilience despite being composed of structurally inferior, weak building blocks, hydrogen bonds.

**Table 1 | Elastic properties of  $\beta$ -sheet nanocrystals as obtained from classical molecular dynamics, experimental results and DFT calculations.**

Approach	Young's modulus (GPa)	Shear modulus (GPa)
Molecular dynamics (this study)	22.6	4.6
Experiment <sup>35,36</sup> (combination of tensile tests, torsion tests and X-ray diffraction)	16–28	2–4*
Density functional theory (this study)	36.45	10.32

\*Experimental measurements of the shear modulus not carried out on individual  $\beta$ -sheet nanocrystals in silk.

given nanocrystal size  $L$ . This scaling implies that modulating the  $\beta$ -strand length could result in more rigid, tougher and more resilient structures. Specifically, the model predicts that for any given nanocrystal length  $L$ , a minimum strand length  $h$  could be found to reach a desired high level of  $s$ .

However, as shown in earlier studies, the effectiveness of each  $\beta$ -strand to carry homogeneous load under shear is limited, and by itself is a function of the strand length  $h$  (refs 13, 38). Although small groups of hydrogen bonds in  $\beta$ -strands can indeed work cooperatively under homogeneous shear, this mechanism breaks down beyond a critical number of hydrogen bonds, at  $N^* \approx 4$  (or equivalently, a critical strand length  $h^* = N^*L_0$ ), owing to a competition between entropic elasticity of the chain and the energetics of hydrogen bonds that will lead to localized failure within each  $\beta$ -strand<sup>13,38</sup> (Fig. 5a and Supplementary Fig. S2 for a visualization of this effect). Most importantly, noting this limitation

on  $h$ , the nanocrystal size cannot be increased arbitrarily, and a critical nanocrystal size  $L^*$  that provides the best overall performance emerges. We estimate critical dimensions  $h^* \approx 1\text{--}2$  nm and  $L^* \approx 2\text{--}4$  nm, defining length scales at which all hydrogen bonds in the nanocrystal gain a strong character through cooperativity (Fig. 5). Notably, these critical dimensions are in agreement with experimental evidence that suggests that poly-Ala and poly-(Gly-Ala) repeats typically span 4–12 amino acids (that is, in the range of  $h = 1\text{--}3$  nm). We note that cooperativity of hydrogen bonds during the formation of  $\beta$ -sheet nanocrystals differs from cooperativity of hydrogen bonds under mechanical load. This is due to the fact that the latter depends strictly on the stress state of the hydrogen bonds as shown here, which is also true for other  $\beta$ -sheet protein structures<sup>13,20</sup>.

The main conclusion from the materiomics studies put forth here is that the nanoscale confinement of  $\beta$ -sheet nanocrystals in silks has a fundamental role in achieving great stiffness, resilience and fracture toughness at the molecular level of the structural hierarchy of silks, suggesting that smaller nanocrystals are stronger and tougher. In contrast to conventional belief, cooperative failure of hydrogen bonds cannot be presumed *a priori*. Rather, the existence of cooperativity depends quite strongly on the size of the crystals and breaks down once  $\beta$ -sheet nanocrystals exceed a critical size. Smaller  $\beta$ -strand nanocrystals provide a greater stiffness and fracture resistance, as they are predominantly loaded in uniform shear, which leads to cooperative rupture of hydrogen bonds and stick–slip energy dissipation mechanisms (Fig. 4). Similar stick–slip mechanisms exist in other biological materials (for example, wood or bone), and are also observed in metals in the form of dislocations that provide ductility<sup>13,38–42</sup>. Further contributions to the macroscale behaviour of silk could arise from higher-order effects owing to the hierarchical structure of the material<sup>15,39,40,42</sup>. As bending is a fundamental mode of deformation of  $\beta$ -sheet nanocrystals that can be thermally excited, our findings could also be important for their thermodynamical stability.

From a slightly different point of view, the generation of a nanocomposite structure (Fig. 5b) can be regarded as the deliberate placement of defects, which effectively results in flaw tolerance<sup>43</sup>. Larger  $\beta$ -sheet nanocrystals are softer and fail catastrophically at much lower forces owing to crack-like flaw formation, as visualized directly in Fig. 2. This catastrophic breakdown leads to rapid disintegration of silk fibres, which is further enhanced owing to easier access of competing water molecules to hydrogen bonds that facilitate rupture<sup>25,44</sup>. This implies that silks with larger nanocrystals are weaker, in agreement with experimental studies<sup>6</sup>. Specifically, our results explain experimental findings that the reduction of the nanocrystal dimensions below 3 nm increases the ultimate strength and the modulus multiple-fold<sup>6</sup>. The mechanism underlying these experimental observations could be the brittle nature of larger  $\beta$ -sheet nanocrystals. Initiating failure of small  $\beta$ -sheet nanocrystals requires much higher forces and a significantly larger amount of mechanical energy. Furthermore, smaller crystals feature a self-healing ability until complete rupture occurs, which is attributed to the capacity of hydrogen bonds to reform during stick–slip deformation. This mechanism protects hydrogen bonds from exposure to surrounding water. In the overall mechanical behaviour of silk, strong, tough and mechanically resilient  $\beta$ -sheet nanocrystals provide effective crosslinks that contribute to the extraordinary macroscopic tensile strength and toughness of silks.

We have presented a general method for predicting material properties of macromolecular nanocrystals and the shear transition length scale directly from atomistic simulation. The method uses generic parameters that can be calculated from experiments or atomistic simulations, and is in principle applicable to a broad range of nanostructures, including synthetic materials (for example, polymer, ceramic or metal fibres). Moreover, the values for the stiffness, bending rigidity and shear contribution presented here for  $\beta$ -sheet nanocrystals are also relevant to protein fibres with a similar chemical make-up, such as amyloids,  $\beta$ -solenoids, protein nanotubes or other fibrous  $\beta$ -proteins that consist of assemblies of  $\beta$ -strands and have very high bending rigidity<sup>33</sup>. Indeed, there is evidence that shear effects are important in other biological filaments such as actin bundles and microtubules<sup>32,45</sup>. The stiffness and stability may be improved slightly by controlling side-chain packing and steric zipper formation (for example, poly-Ala versus Gly–Ala repeats). However, the scaling of the shear contributions is not expected to vary considerably because Gly-to-Ala substitutions have been shown to have marginal influence on the mechanical properties of silk nanocrystals<sup>46</sup>.

The size effect revealed here explains an efficient strategy to overcome the intrinsic brittleness and mechanical weakness of hydrogen bonds by confining structures at controlled length scales, which guarantees uniform deformation and concerted failure (Fig. 5). Another consideration is that, given the seemingly simple nature of the amino-acid composition of silk  $\beta$ -sheet nanocrystals, their capacity to resist mechanical perturbation arises not from their specific chemical features but rather from universal features of the protein backbone combined with the high level of control over their structural dimensions. The utilization of weak hydrogen bonds under nanoconfinement illustrates how a weakness is turned into a strength. Most engineered materials rely on strong (for example, covalent) bonding, which requires considerable energy use during material synthesis that can also lead to catastrophic failure once bonds break. In contrast, the use of weak hydrogen bonding facilitates self-assembly at moderate temperatures and provides a built-in capacity to self-heal because broken hydrogen bonds can be reformed.

The application of our findings to the design of synthetic materials could provide us with new material concepts based on inexpensive, abundant constituents and facilitate the development of effective crosslinking domains. As we are not limited techno-

logically by natural building blocks, it may be possible to improve biological materials beyond their natural capacity. For example, protein structures such as  $\beta$ -sheet nanocrystals could be combined with carbon nanostructures such as graphene or carbon nanotubes, and may thereby enable us to develop more effective nanocomposite structures that make excellent nanoscopic properties usable at larger length scales. Other opportunities include the incorporation of mutability, to develop materials with mechanical properties that can be controlled by external cues such as temperature, pH, magnetic or electric fields. In such mechanomutable materials, external cues are used to control the structure of a material at distinct hierarchy levels and thereby switch a material's properties.

## Methods

**Molecular dynamics model.** The coordinates for the molecular model of silk are obtained from the Protein Data Bank with identification code 2slk (ref. 28), where different sized nanocrystals used here are built by truncating the system to four strands and replicating the system by shifting the molecules at a proper distance<sup>28</sup>. The protein structure and coordinate files are created using the psfgen tool in Nanoscale Molecular Dynamics (NAMD)<sup>47</sup> using Chemistry at Harvard Molecular Mechanics (CHARMM) topology and force-field parameter files<sup>48</sup>. The assembly is then minimized and equilibrated in a transferable intermolecular potential 3P explicit water box. Simulations are carried out in an NPT (isothermal–isobaric) ensemble (Langevin piston Nosé–Hoover method). The piston target pressure is set to 1.01325 bar (1 atm) and the temperature is 300 K. The stability of the  $\beta$ -sheet nanocrystal without load applied is verified from hydrogen-bond dynamics as well as root mean squared deviation data obtained from the molecular dynamics trajectory.

**Application of boundary conditions.** Simulations under lateral loading (Fig. 1b) are carried out using the constant force module in NAMD. One end of the nanocrystal is fixed by constraining the motion of the  $C_\alpha$  atoms at the bottom strand of each sheet. The other end of the nanocrystal is deformed by tip loading, where a constant force is applied to the terminal  $C_\alpha$  atom of each strand at the top. For simulating the pull-out scenario (Fig. 1d), we use steered molecular dynamics<sup>25</sup> (SMD) with a constant pulling velocity. The boundary conditions consist of fixing  $C_\alpha$ -atoms on the top and bottom strands with an SMD spring constant  $k = 10 \text{ kcal mol}^{-1} \text{ \AA}^{-2}$  and a displacement rate  $\dot{x} = 0.0005 \text{ \AA ps}^{-1}$ , in line with other recent SMD studies<sup>25</sup>. For the pull-out simulations, the absolute value of the force levels will differ from experimental studies owing to rate effects. On the basis of earlier studies comparing molecular dynamics simulations of  $\beta$ -sheets with single-molecule experiments<sup>14,25</sup>, we estimate that the strength values are lowered by a factor of six at experimental rates, leading to pull-out strengths in the range of 250–400 pN. Indeed, the values incorporating rate effects are in agreement with atomic force microscopy experimental results of the strength of spider silk nanofibres<sup>30</sup>. The comparison of the influence of the crystal size on strength and toughness, the focus of the study reported in this article, is independent of the specific rate as confirmed by further simulations carried out at varying SMD deformation rates ( $\nu = 0.0005 - 0.02 \text{ \AA ps}^{-1}$ ). Whereas the measured values of the rupture force vary with rate, the length scale in which the stick–slip mechanism emerges is observed to be rate independent.

**Continuum theory.** Considering pure bending, the deformation of the tip is:

$$\delta_{\text{tip}} = \frac{PL^3}{3EI} \quad (2)$$

where  $P$  is the total applied force,  $E$  is the elastic modulus and  $I$  is the second moment of area around the bending axis. By defining an effective stiffness  $k_{\text{eff}} = P/\delta_{\text{tip}}$ , we compare the size dependence of the stiffness with the results obtained from atomistic simulations (for small forces,  $k_{\text{eff}}$  is independent of the force value). As the pure bending theory fails to describe the results of our simulations, we consider an extended beam model that includes the effects of shear deformation<sup>34</sup>. Incorporating shear effects, equation (2) becomes:

$$\delta_{\text{tip}} = \frac{PL}{D_T} + \frac{PL^3}{3D_B} \quad (3)$$

The effective stiffness is given as:

$$k_{\text{eff}}(L) = \frac{P}{\delta_{\text{tip}}} = \left( \frac{L}{D_T} + \frac{L^3}{3D_B} \right)^{-1} \quad (4)$$

The ratio of the first and second terms in equation (3) quantifies the relative importance of shear contributions in the deformation for a given beam with

constant length and material properties (defined as shear contribution ratio  $s$  in equation (1)). Cross-sectional dimensions  $b = 1.37$  nm and  $h = 2.23$  nm are used in the calculation of the moduli values (these values are based on a geometric analysis of the atomic coordinates).

The results from bending and pull-out simulations use different crystal lengths owing to the fact that an odd number of strands is necessary to achieve symmetric loading conditions of the system in pull-out simulations, where force is applied not to the tip but to a central strand. In bending simulations, we consider  $\beta$ -sheet nanocrystal sizes that range from  $L = 1.87$  nm to  $L = 7.04$  nm. Whereas for pull-out simulations, the  $\beta$ -sheet nanocrystal sizes range from  $L = 1.87$  to  $L = 6.56$  nm as provided in the legends of Fig. 3 and Fig. 4. In Fig. 3c, all curves are normalized with respect to the size of each crystal. In Fig. 4b–d the solid lines indicate smoothing spline curves, which are used for guidance.

**Tip displacement and displacement profile analysis.** The purpose of the analysis shown in Fig. 3a is to investigate whether or not a pure bending or combined bending/shear model can describe the entire range of  $\beta$ -sheet nanocrystal stiffnesses observed in the simulation. The result from the analysis shown in Fig. 3a is that a combined shear-bending model provides a much better fit to the overall data. As the fits depicted in Fig. 3a are based solely on tip displacements, we compute refined fits to each displacement profile starting from the initial estimates of the material constants obtained from the overall fit. The purpose of the extended analysis, shown as continuous lines in Fig. 3c, is to extract refined material parameters that are based on the entire set of displacement data for each nanocrystal size considered. The fitted material parameters are consistent with the parameters obtained from the overall fit to the tip displacements shown in Fig. 3a, and are within the 95% confidence range of those parameters. Moreover, the agreement of the shear contribution ratio  $s$  with the fit from Fig. 3a (red curve in Fig. 3b) with refined values (discrete points in Fig. 3b) is very good, supporting the fact that the shear contribution ratios  $s$  do not vary significantly whether a refined fit or an overall fit is used. The distinction between bending and combined bending-shear fits to the overall tip displacement curves is shown in Supplementary Fig. S3. In line with the results shown in Fig. 3a, the plot confirms that pure bending fits to the overall data cannot explain all the curves, and that the addition of a shear term in the combined bending-shear model improves all of the individual displacement profiles.

**Density functional theory.** DFT using the generalized gradient approximation with the Perdew–Burke–Ernzerhof functional for exchange–correlation<sup>49</sup> is carried out using the SIESTA code<sup>50</sup>. Double-zeta polarized basis sets are used for electron orbitals (energy shift 0.15 Ryd). A cutoff of 250 Ryd is used for the charge mesh grid. We consider an antiparallel  $\beta$ -sheet nanocrystal as shown in Supplementary Fig. S1a. Atomic coordinates and lattice constants are optimized using the conjugated gradient algorithm. Criteria for force and stress convergence are 0.01 eV  $\text{\AA}^{-1}$  and 0.01 GPa. The elastic constants are calculated by considering a two-dimensional Voigt stress–strain relation:

$$\begin{bmatrix} \sigma_1 \\ \sigma_2 \\ \sigma_3 \end{bmatrix} = \begin{bmatrix} C_{11} & C_{12} & C_{13} \\ C_{21} & C_{22} & C_{23} \\ C_{31} & C_{32} & C_{33} \end{bmatrix} \begin{bmatrix} \varepsilon_1 \\ \varepsilon_2 \\ \varepsilon_3 \end{bmatrix}$$

where the indices 1 and 2 correspond to the  $z$  and  $y$  directions along the backbone ( $z$ ) and the hydrogen-bond direction ( $y$ ). In Voigt notation,  $\sigma_3 = \sigma_{zy}$ , and  $\varepsilon_3 = 2\varepsilon_{zy}$ . By applying uniaxial tension in the  $z$  and  $y$  directions ( $\varepsilon_1 = \lambda$ ,  $\varepsilon_2 = 0$ ,  $\varepsilon_3 = 0$  and  $\varepsilon_1 = 0$ ,  $\varepsilon_2 = \lambda$ ,  $\varepsilon_3 = 0$ ) and pure shear ( $\varepsilon_1 = 0$ ,  $\varepsilon_2 = 0$ ,  $\varepsilon_3 = \lambda$ ), the elastic tensor  $C_{ij}$  is determined by fitting the stress–strain relation to a linear function. Supplementary Fig. S1b and the right-hand snapshot shown in Fig. 1a plots the electron density distributions in the  $\beta$ -sheet nanocrystal, showing significant charge accumulation at the oxygen atom and along the direction of hydrogen bonds.

For further details, see the Supplementary Information.

Received 12 November 2009; accepted 25 January 2010;  
published online 14 March 2010

## References

1. Becker, N. *et al.* Molecular nanosprings in spider capture-silk threads. *Nature Mater.* **2**, 278–283 (2003).
2. Shao, Z. Z. & Vollrath, F. Materials: Surprising strength of silkworm silk. *Nature* **418**, 741–741 (2002).
3. Vollrath, F. & Knight, D. P. Liquid crystalline spinning of spider silk. *Nature* **410**, 541–548 (2001).
4. Vepari, C. & Kaplan, D. L. Silk as a biomaterial. *Prog. Polymer Sci.* **32**, 991–1007 (2007).
5. Termonia, Y. Molecular modeling of spider silk elasticity. *Macromolecules* **27**, 7378–7381 (1994).
6. Du, N. *et al.* Design of superior spider silk: From nanostructure to mechanical properties. *Biophys. J.* **91**, 4528–4535 (2006).
7. Lee, S. M. *et al.* Greatly increased toughness of infiltrated spider silk. *Science* **324**, 488–492 (2009).
8. Rammensee, S., Slotta, U., Scheibel, T. & Bausch, A. R. Assembly mechanism of recombinant spider silk proteins. *Proc. Natl Acad. Sci. USA* **105**, 6590–6595 (2008).
9. Hayashi, C. Y., Shipley, N. H. & Lewis, R. V. Hypotheses that correlate the sequence, structure, and mechanical properties of spider silk proteins. *Int. J. Biol. Macromol.* **24**, 271–275 (1999).
10. Lefevre, T., Rousseau, M. E. & Pezolet, M. Protein secondary structure and orientation in silk as revealed by Raman spectromicroscopy. *Biophys. J.* **92**, 2885–2895 (2007).
11. van Beek, J. D., Hess, S., Vollrath, F. & Meier, B. H. The molecular structure of spider dragline silk: Folding and orientation of the protein backbone. *Proc. Natl Acad. Sci. USA* **99**, 10266–10271 (2002).
12. Thiel, B. L., Guess, K. B. & Viney, C. Non-periodic lattice crystals in the hierarchical microstructure of spider (major ampullate) silk. *Biopolymers* **41**, 703–719 (1997).
13. Keten, S. & Buehler, M. J. Geometric confinement governs the rupture strength of H-bond assemblies at a critical length scale. *Nano Lett.* **8**, 743–748 (2008).
14. Keten, S. & Buehler, M. J. Asymptotic strength limit of hydrogen bond assemblies in proteins at vanishing pulling rates. *Phys. Rev. Lett.* **100**, 198301 (2008).
15. Rousseau, M. E., Lefevre, T., Beaulieu, L., Asakura, T. & Pezolet, M. Study of protein conformation and orientation in silkworm and spider silk fibers using Raman microspectroscopy. *Biomacromolecules* **5**, 2247–2257 (2004).
16. Grubb, D. T. & Jelinski, L. W. Fiber morphology of spider silk: The effects of tensile deformation. *Macromolecules* **30**, 2860–2867 (1997).
17. Rief, M., Gautel, M., Oesterhelt, F., Fernandez, J. M. & Gaub, H. E. Reversible unfolding of individual titin immunoglobulin domains by AFM. *Science* **276**, 1109–1112 (1997).
18. Lee, E. H., Gao, M., Pinotsis, N., Wilmanns, M. & Schulten, K. Mechanical strength of the titin Z1Z2-telethonin complex. *Structure* **14**, 497–509 (2006).
19. Marszalek, P. E. *et al.* Mechanical unfolding intermediates in titin modules. *Nature* **402**, 100–103 (1999).
20. Brockwell, D. J. *et al.* Pulling geometry defines the mechanical resistance of a beta-sheet protein. *Nature Struct. Biol.* **10**, 731–737 (2003).
21. Eom, K., Li, P. C., Makarov, D. E. & Rodin, G. J. Relationship between the mechanical properties and topology of cross-linked polymer molecules: Parallel strands maximize the strength of model polymers and protein domains. *J. Phys. Chem. B* **107**, 8730–8733 (2003).
22. Sulkowska, J. I. & Cieplak, M. Mechanical stretching of proteins—a theoretical survey of the Protein Data Bank. *J. Phys. Condens. Matter* **19**, 283201 (2007).
23. Buehler, M. J. & Yung, Y. C. Deformation and failure of protein materials in physiologically extreme conditions and disease. *Nature Mater.* **8**, 175–188 (2009).
24. Schwaiger, I., Sattler, C., Hostetter, D. R. & Rief, M. The myosin coiled-coil is a truly elastic protein structure. *Nature Mater.* **1**, 232–235 (2002).
25. Sotomayor, M. & Schulten, K. Single-molecule experiments *in vitro* and *in silico*. *Science* **316**, 1144–1148 (2007).
26. Ma, B. & Nussinov, R. Molecular dynamics simulations of the unfolding of beta(2)-microglobulin and its variants. *Protein Eng.* **16**, 561–575 (2003).
27. Brooks, C. L. Methodological advances in molecular-dynamics simulations of biological-systems. *Curr. Opin. Struct. Biol.* **5**, 211–215 (1995).
28. Fossey, S. A., Nemethy, G., Gibson, K. D. & Scheraga, H. A. Conformational energy studies of beta-sheets of model silk fibroin peptides 1. Sheets of poly(Ala–Gly) chains. *Biopolymers* **31**, 1529–1541 (1991).
29. Shao, Z. Z. & Vollrath, F. The effect of solvents on the contraction and mechanical properties of spider silk. *Polymer* **40**, 1799–1806 (1999).
30. Oroudjev, E. *et al.* Segmented nanofibers of spider dragline silk: Atomic force microscopy and single-molecule force spectroscopy. *Proc. Natl Acad. Sci. USA* **99**, 6460–6465 (2002).
31. Sirichaisit, J., Brookes, V. L., Young, R. J. & Vollrath, F. Analysis of structure/property relationships in silkworm (*Bombyx mori*) and spider dragline (*Nephila edulis*) silks using Raman spectroscopy. *Biomacromolecules* **4**, 387–394 (2003).
32. Pampaloni, F. *et al.* Thermal fluctuations of grafted microtubules provide evidence of a length-dependent persistence length. *Proc. Natl Acad. Sci. USA* **103**, 10248–10253 (2006).
33. Knowles, T. P. *et al.* Role of intermolecular forces in defining material properties of protein nanofibrils. *Science* **318**, 1900–1903 (2007).
34. Connor, J. J. *MIT-Prentice Hall Series on Civil, Environmental, and Systems Engineering* xiv 53–56 (Prentice Hall Pearson Education, 2003).
35. Krasnov, I. *et al.* Mechanical properties of silk: Interplay of deformation on macroscopic and molecular length scales. *Phys. Rev. Lett.* **100**, 048104 (2008).
36. Philip, M. C. *et al.* Mechanical and thermal properties of dragline silk from the spider *Nephila clavipes*. *Polym. Adv. Technol.* **5**, 401–410 (1994).
37. Ko, F. K. & Jovicic, J. Modeling of mechanical properties and structural design of spider web. *Biomacromolecules* **5**, 780–785 (2004).
38. Keten, S. & Buehler, M. J. Strength limit of entropic elasticity in beta-sheet protein domains. *Phys. Rev. E* **78**, 061913 (2008).

39. Fratzl, P. & Weinkamer, R. Nature's hierarchical materials. *Prog. Mater. Sci.* **52**, 1263–1334 (2007).
40. Hartmann, M. A. & Fratzl, P. Sacrificial ionic bonds need to be randomly distributed to provide shear deformability. *Nano Lett.* **9**, 3603–3607 (2009).
41. Keckes, J. *et al.* Cell-wall recovery after irreversible deformation of wood. *Nature Mater.* **2**, 810–814 (2003).
42. LeDuc, P. R. & Robinson, D. N. Using lessons from cellular and molecular structures for future materials. *Adv. Mater.* **19**, 3761–3770 (2007).
43. Gao, H. J., Ji, B. H., Jager, I. L., Arzt, E. & Fratzl, P. Materials become insensitive to flaws at nanoscale: Lessons from nature. *Proc. Natl Acad. Sci. USA* **100**, 5597–5600 (2003).
44. Porter, D. & Vollrath, F. The role of kinetics of water and amide bonding in protein stability. *Soft Matter*. **4**, 328–336 (2008).
45. Claessens, M. M. A. E., Bathe, M., Frey, E. & Bausch, A. R. Actin-binding proteins sensitively mediate F-actin bundle stiffness. *Nature Mater.* **5**, 748–753 (2006).
46. Xiao, S. B., Stacklies, W., Cetinkaya, M., Markert, B. & Grater, F. Mechanical response of silk crystalline units from force-distribution analysis. *Biophys. J.* **96**, 3997–4005 (2009).
47. Nelson, M. T. *et al.* NAMD: A parallel, object oriented molecular dynamics program. *Int. J. Supercomputer Appl. High Performance Comput.* **10**, 251–268 (1996).
48. MacKerell, A. D. *et al.* All-atom empirical potential for molecular modelling and dynamics studies of proteins. *J. Phys. Chem. B* **102**, 3586–3616 (1998).
49. Perdew, J. P., Burke, K. & Ernzerhof, M. Generalized gradient approximation made simple. *Phys. Rev. Lett.* **77**, 3865–3868 (1996).
50. Soler, J. M. *et al.* The SIESTA method for *ab initio* order-*N* materials simulation. *J. Phys. Condens. Matter* **14**, 2745–2779 (2002).

### Acknowledgements

This work was supported by the Office of Naval Research (N00014-08-1-00844). Further support from the National Science Foundation (CMMI-0642545 and MRSEC DMR-0819762), the Army Research Office (W911NF-06-1-0291), DARPA (HR0011-08-1-0067) and the MIT Energy Initiative is acknowledged. B.I. acknowledges support from MIT's UROP and the MISTI-Germany programme. This research was supported by an allocation of advanced computing resources supported by the National Science Foundation (TeraGrid, grant no. TG-MSS080030). Further simulations have been carried out at MIT's Laboratory for Atomistic and Molecular Mechanics. The authors thank J. J. Connor and T. Radford at MIT for fruitful discussions.

### Author contributions

S.K. and M.J.B. designed the research and analysed the results. S.K., Z.X. and B.I. carried out atomistic and molecular simulations. S.K., Z.X. and M.J.B. wrote the paper.

### Additional information

The authors declare no competing financial interests. Supplementary information accompanies this paper on [www.nature.com/naturematerials](http://www.nature.com/naturematerials). Reprints and permissions information is available online at <http://npg.nature.com/reprintsandpermissions>. Correspondence and requests for materials should be addressed to M.J.B.